Synthesis of Ni Nanoparticles with Controllable Magnetic Properties by Atmospheric Pressure Microplasma Assisted Process

Liangliang Lin, Sirui Li, and Volker Hessel
Dept. of Chemical Engineering and Chemistry, Micro Flow Chemistry and Process Technology, Eindhoven University of Technology, P.O. Box 513, Eindhoven MB 5600, the Netherlands

Sergey A. Starostin
FUJIFILM Manufacturing Europe, Tilburg Research Labs, B.V, P.O. Box 90156, Tilburg, the Netherlands

R. Lavrijsen
Dept. of Applied Physics, Eindhoven University of Technology, P.O. Box 513, Eindhoven MB 5600, the Netherlands

Wei Zhang
Dept. of Chemical Engineering and Chemistry, Micro Flow Chemistry and Process Technology, Eindhoven University of Technology, P.O. Box 513, Eindhoven MB 5600, the Netherlands

School of Marine Science and Engineering, Hebei University of Technology, Tianjin 300130, China

DOI 10.1002/aic.16054
Published online in Wiley Online Library (wileyonlinelibrary.com)

An atmospheric pressure microplasma technique is demonstrated for the gas phase synthesis of Ni nanoparticles by plasma-assisted nickelocene dissociation at different conditions. The dissociation process and the products are characterized by complementary analytical methods to establish the relationship between operational conditions and product properties. The innovation is to show proof-of-principle of a new synthesis route which offers access to less costly and less poisonous reactant, a higher quality product, and a simple, continuous and pre/post treatment-free manner with chance for fine-tuning "in-flight." Results show that Ni nanoparticles with controllable magnetic properties are obtained, in which flexible adjustment of product properties can be achieved by tuning operational parameters. At the optimized condition only fcc Ni nanoparticles are formed, with saturation magnetization value of 44.4 mAm^2/g. The upper limit of production rate for Ni nanoparticles is calculated as 4.65 $\times$ 10^{-3} g/h using a single plasma jet, but the process can be scaled-up through a microplasma array design. In addition, possible mechanisms for plasma-assisted nickelocene dissociation process are discussed. © 2017 American Institute of Chemical Engineers *AIChE J*, 00: 000–000, 2017
Keywords: microplasma, microreactor, plasma technology, Ni nanoparticles, magnetic properties

Introduction

Owing to their unique magnetic properties, iron group nanoparticles (Fe, Co, and Ni) enable promising applications in high density recording, medical imaging, ferrofluids, drug delivery, and magnetic thermal therapy.[1–3] Presently there is an increasing interest to Ni nanoparticles as they show promise in the field of magnetic hyperthermia for cancer treatment. This is induced by the synergistic combination of characteristics such as high saturation magnetization (M_s) value, excellent biocompatibility, slow oxidation rate compared to Fe and Co as well as cytotoxicity against cancerous cells.[4,5]

It is well known that material properties depend critically on particle size, structure and morphology. For example, the surface plasmon resonance of gold nanoparticles shows a red shift with increasing particle size, resulting in a considerable variation in optical properties.[6] Iron oxide nanoparticles of maghemite structure (γ-Fe_2O_3) show excellent superparamagnetic behavior, in contrast to the antiferromagnetic nature of hematite (α-Fe_2O_3).[7] Also, the hyperthermia therapy efficacy of Ni nanoparticles is affected by several parameters: (1) Composition. The existence of impurities will significantly reduce their magnetic performance. (2) Particle size. The saturation magnetization of Ni nanoparticles is size-dependent, which decreases with decreasing particle size.[8] (3) Structure.

Additional Supporting Information may be found in the online version of this article.

Correspondence concerning this article should be addressed to V. Hessel at v.hessel@tue.nl.

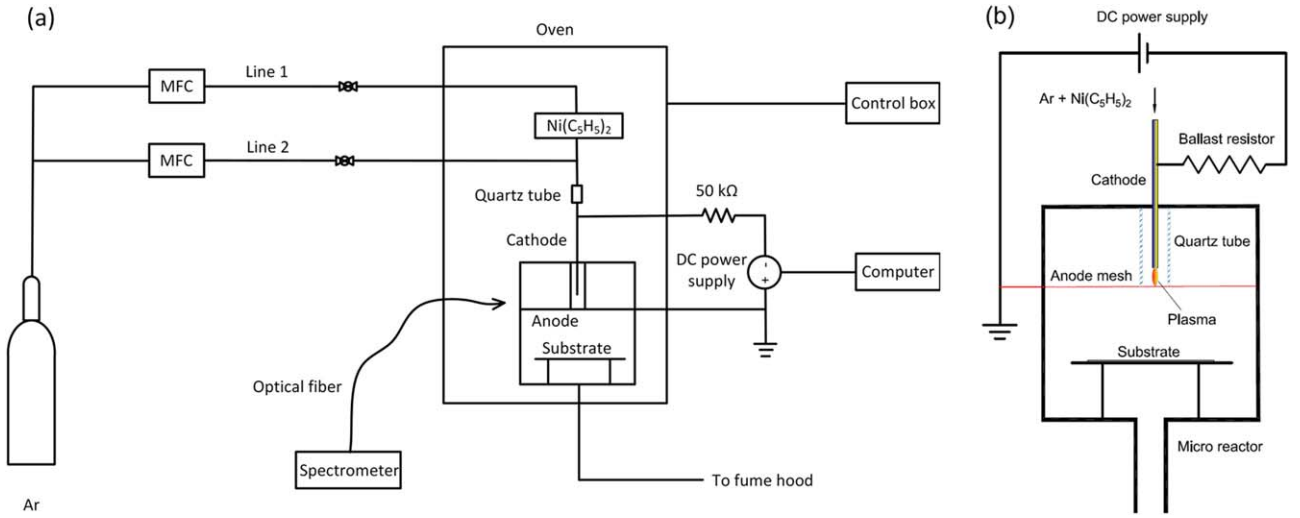

Figure 1. Schematic diagram of (a) the microplasma setup and (b) the microreactor for magnetic Ni NPs synthesis.

[Color figure can be viewed at wileyonlinelibrary.com]

The face-centered-cubic (fcc) phase Ni nanoparticles show better hyperthermia properties and have much higher M_s values ($\sim$48.5 mAm^2/g) compared with the hexagonal-close-packed (hcp) phase (< 1 mAm^2/g).[9] As magnetic properties of Ni nanoparticles are closely related to those parameters, the manipulation of particle size, morphology, and crystalline phase will allow us to have a precise control of their properties that can be optimized for specific applications.

The synthesis of Ni nanoparticles has been widely studied over the past decades, including a variety of novel or well-established methods such as microemulsion, sputtering, pyrolysis, ultrasound-assisted, solution combustion, chemical reduction, and sol-gel process.[10,11] However, these approaches are generally multisteps and time consuming, requiring pre/posttreatments such as separation, washing or annealing to improve purity and crystallinity. Flexible control over composition, structure, and particle size during these processes is difficult to achieve, with the mechanisms poorly understood. Moreover, a great concern for bio-application is toxic chemicals are involved (e.g., reducing agents, solvents, catalysts, or surfactants), leading to undesirable hazardous interactions with biological systems and the environment. Therefore, the controllable synthesis of Ni nanoparticles with desired properties in a simple, continuous, nontoxic, and efficient way is still a challenge.

As a new generation technique for nanomaterial synthesis, the microplasma-assisted approach not only provides a rapid, cost-effective and continuous route to prepare high quality nanoparticles, but also simplifies the preparation process by omitting complex pre/posttreatments as well as expensive vacuum equipment.[12–14] Preceding studies have shown that particle size, morphology, composition, and microstructure can be tuned through processing parameters.[15] Moreover, as reactions take place in the gas phase, hazardous wet chemistry is not involved, rendering it to be a promising protocol for nanomaterial fabrication, especially for bio-application purpose.

With the motivation to synthesize Ni nanoparticles of controllable magnetic properties in a simple, continuous and environmental friendly way, a microplasma-assisted approach is adopted in this study. We first sought to test a hypothesis that the properties of Ni nanoparticles can be controlled and tuned by adjusting the power dissipated in the plasma. As Ni nanoparticles of fcc phase are more stable than hcp phase at high temperatures, increasing the plasma power will lead to an increased gas temperature, inducing a structure transition from the hcp to fcc phase. Meanwhile, the plasma power also affects the electron density and energy distribution function, which affects precursor dissociation and particle nucleation processes, resulting in products of different size, composition, and morphology. In addition to plasma power, another hypothesis is that the control over properties should be achieved by adjusting the precursor concentration, through which particle size, morphology, and composition are influenced. In this study, the relationship between experimental conditions and product composition, size, morphology as well as structure is investigated to correlate with their magnetic behavior and to obtain a precise control over those parameters. Furthermore, possible mechanisms for the plasma-assisted nickelocene dissociation are discussed to provide an insight into the complex process.

Experimental

Synthesis

In this research, Ni nanostructures are synthesized in a specially designed microreactor by an atmospheric pressure microplasma setup (Figure 1). Briefly, nickelocene ($Ni(cp)_2$ or $Ni(C_5H_5)_2$, Acros-Organics) vapors were delivered into plasma with a continuous argon flow in line 1. A separate argon flow in line 2 acting as dilution gas was designed to adjust the precursor concentration. These two MFC controlled flows were then mixed before being injected into the microreactor. During all experiments the total gas flow rate was kept constant at 100 sccm. The $Ni(cp)_2$ vapor concentration was derived from vapor pressure data[16] combined with Dalton's Law and Amagat's Law.[17] To avoid precursor condensation, the gas lines and the microreactor were assembled inside a thermostat oven with a fixed temperature of 323 K. A commercial DC power supply (Matsusada Precision, Model AU-10R30) was employed to generate and sustain the plasma between a stainless steel (SS) capillary tube and a SS mesh, with a 2 mm gap. Experimental values of discharge current and voltage were automatically logged using a LabVIEW based program. The reaction products were collected by placing a SS mesh downstream of the aerosol.

Table 1. Processing Parameters for the Synthesis of Ni Nanoparticles

Condition	Plasma Power (W)	Line 1 (sccm)	Line 2 (sccm)	Current (mA)	Voltage (V)	$Ni(cp)_2$ Concentration (ppm)	Crystalline Size and Composition[a] (nm)	M_s (mAm^2/g)	Throughput[b] (Single Jet) (g/h)
1	1.3	30	70	6.0	220	35.0	9.2 nm (fcc, hcp, C)	16.1	4.65×10^{-3}
2	2.0	30	70	9.3	216	35.0	17.4 nm (fcc, hcp)	26.4	4.65×10^{-3}
3	2.7	30	70	12.8	210	35.0	22.8 nm (fcc, hcp)	34.9	4.65×10^{-3}
4	3.4	30	70	16.2	207	35.0	27.0 nm (fcc)	44.4	4.65×10^{-3}
5	1.3	15	85	6.0	220	17.5		22.8	2.33×10^{-3}
6	2.0	15	85	9.3	216	17.5		25.4	2.33×10^{-3}
7	2.7	15	85	12.8	210	17.5		33.5	2.33×10^{-3}
8	3.4	15	85	16.2	207	17.5		38.4	2.33×10^{-3}

[a]The crystal size and phase composition is derived from the XRD results using Scherrer formula; fcc (face-centered-cubic Ni), hcp (hexagonal-close-packed Ni), C (crystalline carbon).
[b]Throughput is calculated based on the $Ni(cp)_2$ feeding rate, with an assumption of 100% precursor conversion using a single plasma jet.

Systematic experiments were performed to study the influence of processing parameters on the products and their magnetic properties. A detailed list of processing parameters and product properties is given in Table 1. First, the effect of discharge power was investigated, when the plasma power was varied from 1.3 to 3.4 W while keeping a constant precursor concentration (35 ppm, condition 1–4). Next, the influence of precursor concentration was studied by operating the plasmas in the same power range but with half the precursor concentrations (17.5 ppm, condition 5–8). The typical procedure was as follows: a discharge was ignited in pure argon. After stabilization, $Ni(cp)_2$ vapors were delivered into the discharge through line 1 at a fixed gas flow rate. Meanwhile, the gas flow rate of line 2 was adjusted to maintain the total gas flow at 100 sccm. After a set process time (2 h), line 1 was closed and the plasma was sustained for a while in pure argon to flush possible $Ni(cp)_2$ residues, before switching off the discharge.

Characterization

Optical emission spectroscopy (HR4000, Ocean Optics) with a spectral resolution of 0.91 nm was employed to analyze the $Ni(cp)_2$ dissociation process and to identify specific intermediate radicals existing in the plasma. The emitted light was collected by an optical fiber fixed at 20 mm distance from the electrodes axis. To characterize the morphology of the products, sample images were recorded by a Quanta 3D FEG (FEI) scanning electron microscopy (SEM). The particles size and shape was further characterized using a FEI Tecnai 20 (type Sphera) transmission electron microscope (TEM), with selected-area electron diffraction (SAED) analysis to identify crystalline phases. XRD measurements were performed using a Rigaku Geigerflex X-ray diffractometer (Cu-$K_{\alpha 1}$ radiation, $\lambda = 1.54056$). The average grain size of the Ni nanoparticles was estimated from the highest intensity peak (111) at 44.5° using the Scherrer formula. Magnetic properties of the products were evaluated using a VSM-SQUID magnetometer from Quantum Design (MPMS 3). Hysteresis loops and the saturation magnetization were measured at room temperature. Zero field cooled (ZFC) measurement were performed using the following procedure: the samples were cooled to 5 K in the absence of an external magnetic field. Then a field of 10 mT was applied and the magnetization was measured as a function of temperature up to 300 K. For the field cooled (FC) measurement, samples were cooled to 5 K in the presence of a constant magnetic field of 10 mT, then the magnetization was measured as a function of temperature up to 300 K, while keeping the 10 mT field present.

Results and Discussions

The precursor dissociation process is characterized in situ through OES measurement by recording the emitted spectra and correlating the spectral features with emission peaks of $Ni(cp)_2$ originated radicals. Based on preceding reports[18–22] and NIST Atomic Spectra Database,[23] detailed radiative transition information of species resulted by $Ni(cp)_2$ dissociation process is summarized in Supporting Information Table S1. Figure 2 shows a representative spectrum recorded from a discharge operated at condition 4 to identify the intermediate radicals in plasma. Apart from the dominant argon atomic transitions (Ar I) between highly excited electronic states in the region of 690–850 nm, prominent emission peaks of carbonaceous species corresponding to C_2 Swan bands (467–474 nm [$\Delta v = -1$], 512–520 nm [$\Delta v = 0$], 550–565nm [$\Delta v = +1$]), C_2 Fox-Herzberg bands (285–315 nm) and CH bands (380–390 nm [3900 Å system], 430–435 nm [4300 Å system]) are found in all spectra. Furthermore, low intensity peaks at 657 nm and 340–355 nm are observed in all spectra, which are ascribed to H_α and Ni lines, respectively.[24,25] The presence of emission lines related to $Ni(cp)_2$ fragments proves the decomposition of $Ni(cp)_2$ vapors in the argon discharge.

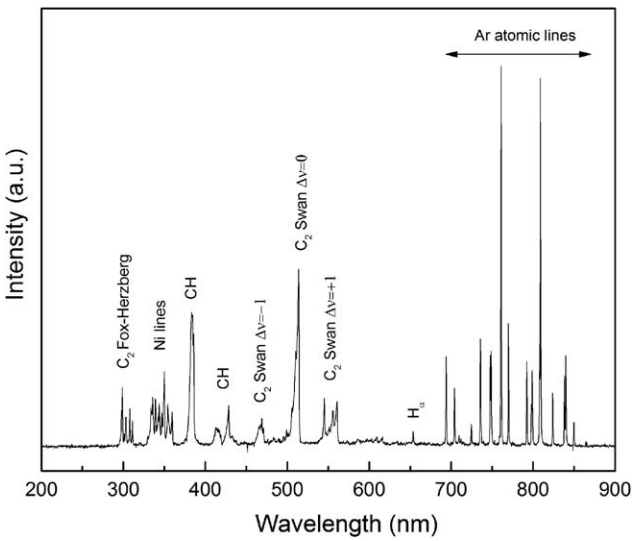

Figure 2. A representative OES spectrum recorded from discharge operated at plasma power of 3.4 W, with $Ni(cp)_2$ concentrations of 35 ppm.

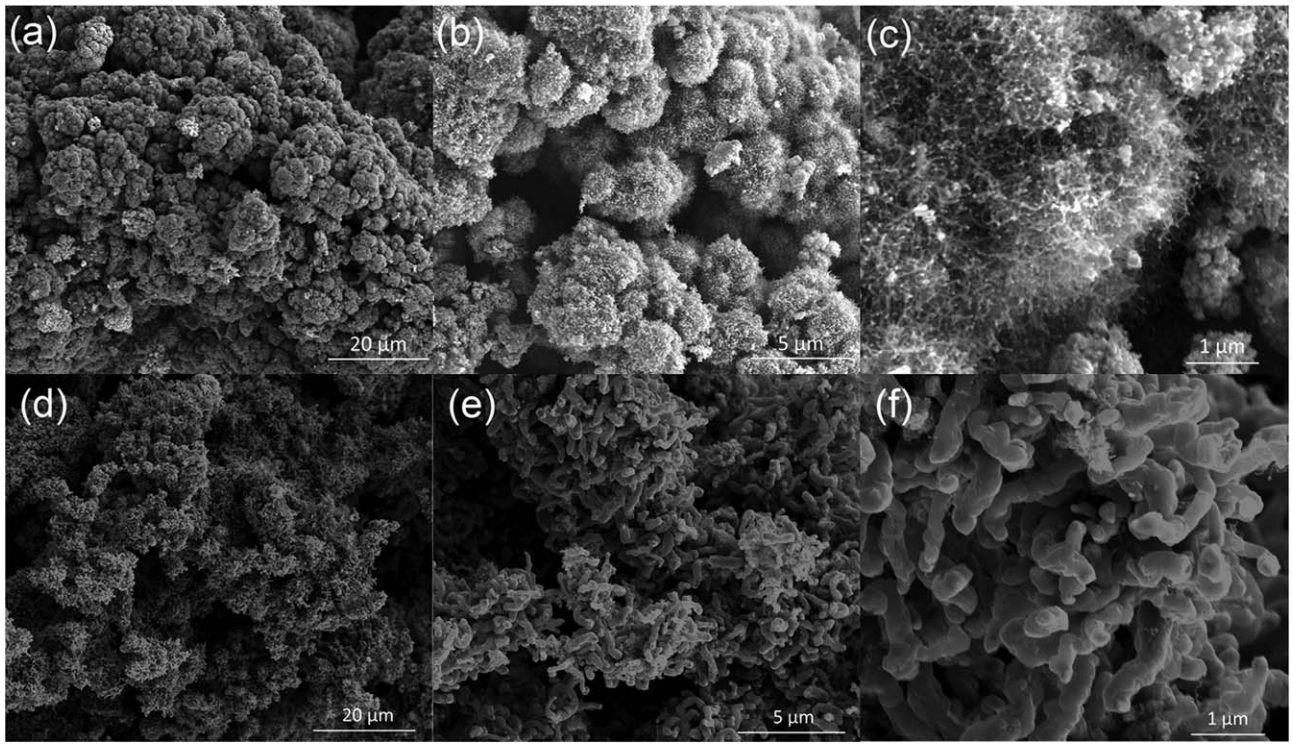

Figure 3. SEM images at different magnification of materials synthesized at plasma power of (a–c) 1.3 W, and (d–f) 3.4 W, with fixed $Ni(cp)_2$ concentration of 35 ppm.

Moreover, to investigate the influence of the plasma power on the dissociation process, spectra recorded from discharges operated at conditions 1–3 are shown in Supporting Information Figures S1a–c. It is clearly observed that the line intensities of the $Ni(cp)_2$ originated fragments and their ratios relative to the argon lines increase with the discharge power, indicating concentration growth of the corresponding excited species. This is probably due to an increased electron density at higher power which, in turn, results in a higher precursor dissociation rate and deeper fragmentation. In addition to the plasma power variation, spectra corresponding to different $Ni(cp)_2$ concentrations are also recorded to study the effect of variation in precursor flow. As shown in Supporting Information Figure S1d–f, for the discharge with a $Ni(cp)_2$ concentration of 11.7 ppm, only barely distinguishable spectral features of $Ni(cp)_2$ fragments are detected. By contrast, their intensities are found to increase significantly with the $Ni(cp)_2$ concentration. This is probably because a higher $Ni(cp)_2$ concentration results in an improved production rate of radiating fragments. Therefore, in the described setup, the precursor dissociation rate can be controlled by tuning the discharge power or by the variation in $Ni(cp)_2$ mass flow.

Ex situ materials characterization starts with SEM analysis to give a general overview of product morphology. Representative images of products synthesized at 1.3 and 3.4 W with 35 ppm $Ni(cp)_2$ vapors are shown in Figure 3 to study the influence of plasma power. Meanwhile, typical images of products obtained at 2.0 and 2.7 W with the same $Ni(cp)_2$ concentration are also provided in Supporting Information Figure S2 for complementary information. It is indicated that the products prepared at 1.3 W are clustered as spherical particles to form coralline-structure morphology. These coralline structures are typically 2–3 μm in diameter and covered with a high density of entangled fibril/felt-like branches. According to previous studies, such branches are attributed to carbon nanotubes (CNTs) growing on the surface of the catalytic nanoparticles.[26] For products synthesized at 2.0 W (Supporting Information Figures S2a–b), small particles of 20–50 nm are clustered together to form cauliflower-like bunches, containing significantly less fibril/felt-like carbon fibers. The further increase of the plasma power to 2.7 W results in well dispersed spherical agglomerations and the absence of entangled fibril/felt-like CNTs (Supporting Information Figures S2c–d). As to products synthesized at 3.4 W, typical bidimensional rod structures are formed by randomly oriented nanoribbons, demonstrating an entirely different morphology, and CNTs totally disappear. The morphology transition from coralline-structure to nanoribbon-structure with increasing temperatures was also observed by Chinnasamy et al.,[27] where a polyol process was used to prepare fcc/hcp phase Ni nanoparticles. Based on the above analysis, the plasma power is shown to have a significant effect on the sample morphology. At high powers nanoparticles tend to agglomerate in rod-like structures, without the formation of CNTs, suggesting that heating contributes to the specific agglomeration of nanoparticles and the inhibition of CNTs.

The influence of precursor concentration on the particle morphology was also investigated using SEM analysis. Representative comparisons are carried out by keeping the plasma powers at 1.3 and 3.4 W while halving the $Ni(cp)_2$ concentration to 17.5 ppm (condition 5 and condition 8). Supporting Information Figures S3a, b shows that products synthesized at condition 5 form a characteristic hydrangea-like morphology. The magnified image reflects the existence of CNTs covering the particle surface. However, their density is much lower compared to products obtained at the double $Ni(cp)_2$ concentration. For products collected at condition 8, particles show irregular shapes and adhere together to form hydrangea-like shapes instead of rod-structures.

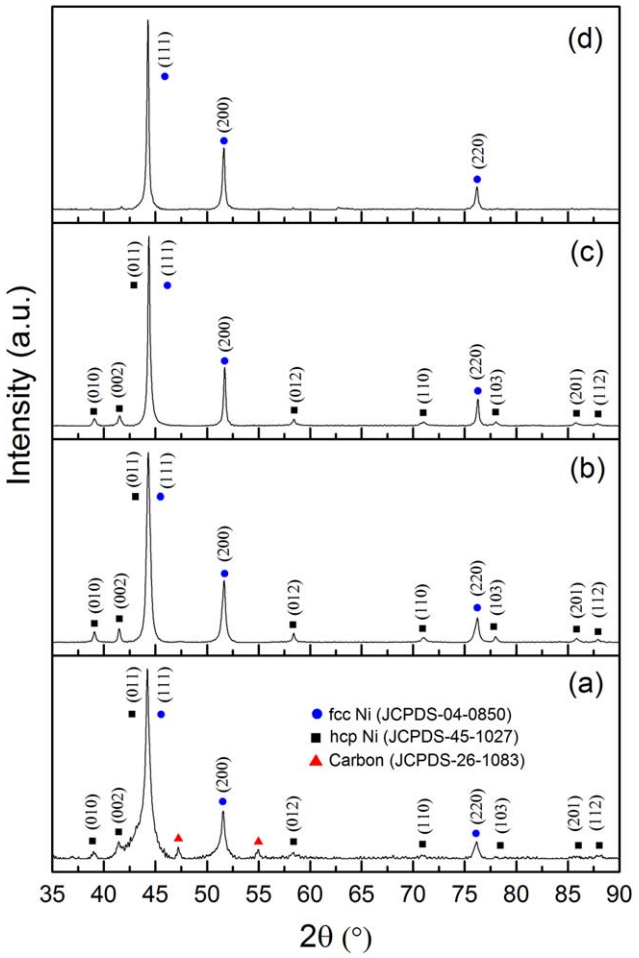

Figure 4. XRD patterns of nanoparticles synthesized at fixed $Ni(cp)_2$ concentration of 35 ppm but with different plasma powers: (a) 1.3 W, (b) 2.0 W, (c) 2.7 W, and (d) 3.4 W.

[Color figure can be viewed at wileyonlinelibrary.com]

Meanwhile, as shown in Supporting Information Figures S3c, d, the particles are smaller and more uniform compared to the particles synthesized at a 35 ppm $Ni(cp)_2$ concentration. Therefore, SEM imaging reveals that the precursor concentration also affects the product morphology and CNTs formation.

The XRD patterns plotted in Figure 4 correspond to products synthesized at condition 1–4. All results indicate a crystalline nature of the as-prepared particles, revealed by distinctive diffraction peaks. The XRD pattern of the condition 1 exhibits three prominent peaks at 2θ values of 44.5°, 51.8°, and 76.4°, which are indexed to the (111), (200), and (220) planes of fcc Ni nanoparticles (JCPDS PDF card #04-0850). Meanwhile, less intensive peaks of the hcp Ni (JCPDS PDF card #45-1027) at 39.1°(010), 41.5°(002), 58.4°(012), 71.0°(110), 78.0°(103), 85.8°(112), 87.9°(201) as well as characteristic carbon peaks at 43.25° and 43.49° are also detected. However, with increasing plasma powers, one can observe that hcp Ni peaks and the relative intensity ratio (RIR) of hcp to fcc Ni phase decrease apparently, indicating the inhibition of hcp Ni nanoparticles. For products obtained at condition 4, negligible hcp Ni are present, with the absence of any characteristic carbon peaks, suggesting the formation of CNTs is totally suppressed. This is in agreement with the SEM results. Furthermore, the narrowing of the peaks with increasing plasma power reflects increase in grain size, and the crystal size and phase composition is listed in Table 1. The XRD results confirm our hypothesis, where a structural transition of Ni nanoparticles from hcp to the fcc phase is observed at high plasma powers. This is because hcp Ni nanoparticles are stable at low temperature, but undergo a transition to the fcc phase above 673 K.[28] The XRD pattern of products synthesized at condition 8 is also shown in Supporting Information Figure S4. It turns out that all hcp Ni peaks vanish, leaving three significant peaks of fcc Ni nanoparticles. Therefore, it is concluded that the structure of products can be tuned by adjusting the precursor concentration.

TEM images of particles synthesized at condition 1–4 are presented to give a better insight of the impact of plasma power on the products. Particles prepared at 1.3 W appear to be spherical, relatively small and quite uniform, with approximate diameters of 5–15 nm (Figures 5a, b). One can also note that abundant CNTs coexisting with Ni nanoparticles, from which carbon lattice fringes are clearly observed in the high-resolution image. The presence of CNTs reconfirms the SEM and XRD results, where fibril/felt-like carbon fibers form a closely packed layer outside the Ni particles. When increasing the plasma power to 2.0 W, relatively larger sized Ni nanoparticles are observed, with much less CNTs incorporated (Supporting Information Figures S5a, b). The SAED pattern shows diffraction rings are perfectly indexed to the (111), (200), (220), and (311) planes of fcc Ni, suggesting that fcc phase Ni nanoparticles are dominant in the products. A gradual increasing trend on particle size and agglomeration is observed as the plasma power rises. Particles appear to be spherical and are estimated to have an average size of 5–20 nm at 2.7 W. Moreover, their lattice fringes can be clearly observed in the high-resolution TEM image (Supporting Information Figures S5c, d). When synthesized at 3.4 W, the particles have even a broader size distribution (5–25 nm). Their morphologies vary from nearly spherical to cubic. Besides, as indicated by the SAED pattern, they prove to be polycrystalline, and the diffraction rings are well assigned to the (111), (200), (220), and (311) planes of fcc Ni. Another noteworthy observation is that no CNTs appear in the products, in accordance with the SEM and XRD results. To give a better understanding of the influence of precursor concentration on particle morphology, TEM images of products synthesized at condition 8 are also provided in Figures 5e, f. Particles are shown to have various shapes (spherical, cubic, oval, and irregular). The size is estimated to be in the range of 4–16 nm, which is smaller and more uniform compared with products obtained at double the precursor concentration (5–25 nm). In addition, the diffraction rings are also indexed to the (111), (200), (220), and (311) planes of fcc Ni nanoparticles, without the appearance of CNTs. However, due to their magnetic properties, the significant agglomeration phenomenon among Ni nanoparticles makes it difficult to derive accurate particle size distributions.

The temperature dependence of magnetization (M-T) curves of hcp Ni nanoparticles is considerably different from the fcc phase, where the hcp phase shows negligible magnetization in ZFC-FC curves, in contrast to the obvious magnetic behavior of fcc Ni nanoparticles.[29,30] Besides, the blocking temperature (T_B) of the hcp Ni nanoparticles is tested to be around 12 K, much lower than that of fcc Ni (above 300 K).[9] A sharp T_B peak always exists in the M-T curves of hcp Ni nanoparticles around 12–13 K, whereas that of fcc Ni nanoparticles is broad and size dependent.[30] To get further information on magnetic

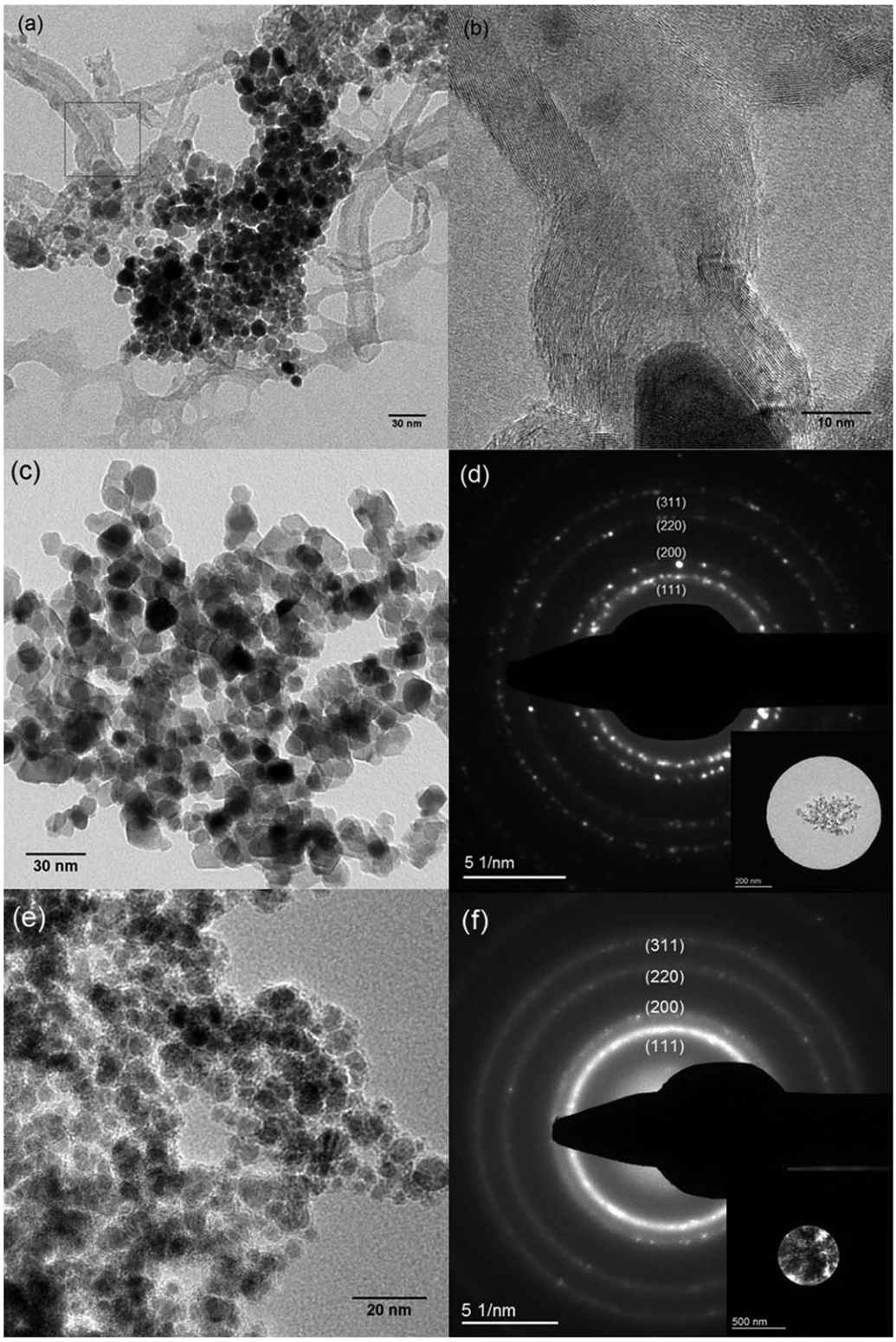

Figure 5. Representative TEM and SAED images of products fabricated at various operation parameters: (a, b) 1.3 W, 35 ppm $Ni(cp)_2$ vapor. (c, d) 3.4 W, 35 ppm $Ni(cp)_2$ vapor. (e, f) 3.4 W, 17.5 ppm $Ni(cp)_2$ vapor.

properties and confirm the correlation between structure and the magnetic behaviors, at first the M-T measurements were performed. Figure 6 shows M-T curves corresponding to products synthesized at condition 1–4. For all samples synthesized in the given conditions, no sharp peaks are observed at $\sim$12 K, and the ZFC magnetization increases with temperature while the FC magnetization is almost constant, which is characteristic M-H behavior of fcc Ni nanoparticles. The bifurcation of ZFC-FC magnetization curves is estimated to be a slightly higher than 300 K, suggesting the products behave ferromagnetically and the blocking temperature is above 300 K. Therefore, this provides an additional proof that fcc Ni nanoparticles are dominant in the products, being consistent with the XRD results.

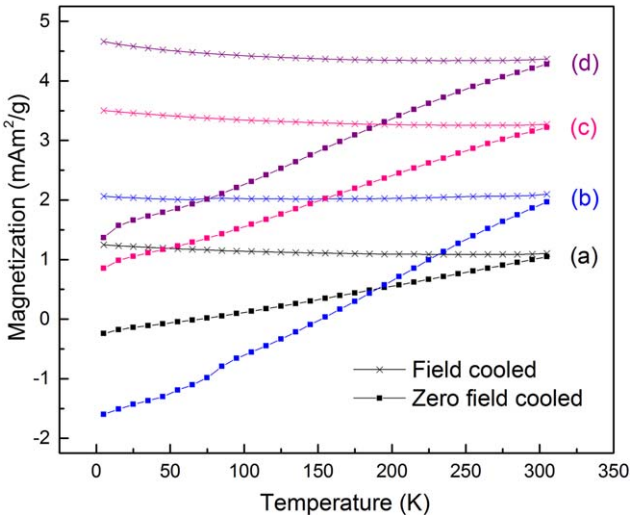

Figure 6. Effect of plasma power on the temperature dependence of magnetization (M-T) curves: (a) 1.3 W, (b) 2.0 W, (c) 2.7 W, and (d) 3.4 W.

[Color figure can be viewed at wileyonlinelibrary.com]

Figure 7 presents the hysteresis (M-H) loops of products synthesized at condition 1–4. All products show ferromagnetic behavior and reach magnetic saturation at an applied magnetic field of around 0.5 T. The M_s increases with the plasma power, from 16.1 mAm^2/g at 1.3 W to 44.4 mAm^2/g at 3.4 W, which is still lower compared to bulk nickel (55 mAm^2/g). The increase of M_s with the plasma power is explained by:

1. The M_s of nanoparticles decreases with decreasing particle size. In the theory, it follows the formula[8]

$$M_s = M_{sb}(1-6t/D)$$

where M_{sb} denotes the magnetic saturation of the bulk nickel, t denotes the thickness of magnetically inactive layer, and D corresponds to the diameter of nanoparticles. A lower plasma power results in smaller-sized nanoparticles, leading to an increased surface-to-volume ratio as well as a higher fraction of magnetically inactive material. Therefore, the M_s of nanoparticles is relatively larger when synthesized at higher plasma powers.

2. Less CNTs are formed at high plasma powers. As a consequence, high purity Ni nanoparticles are obtained, leading to an enhanced M_s. Our results show that CNTs coexisting with Ni nanoparticles at low plasma powers, while are suppressed at high powers. A reasonable explanation is that the Ni nanoparticles generated at lower power are smaller, resulting in larger specific surface area, thus, allowing carbon supersaturation readily. Therefore, they are more active in catalyzing hydrocarbons to form CNTs. This is in agreement with preceding findings, which showed that the CNTs formation rate depended inversely on catalyst size, and no CNTs were formed by catalysts with diameters larger than 7 nm.[31,32]
3. The M_s of fcc Ni are much larger than that of the hcp phase, and they are more stable at high temperatures. The increase of plasma power contributes to the transition of Ni nanoparticles from hcp to fcc phase, resulting in an improved M_s value.

In addition to plasma power, M-H measurements of products obtained at condition 5–8 are also conducted to study the effect of precursor concentration, as illustrated in Supporting Information Figure S6. It is clearly shown that all samples have ferromagnetic behavior, and their M_s increases with plasma power. Compared to products obtained with double $Ni(cp)_2$ concentration, the increasing trend is "milder," from 22.8 mAm^2/g at 1.3 W to 38.4 mAm^2/g at 3.4 W.

Based on experimental results, here we have verified the hypothesis that magnetic properties of Ni nanoparticles can be controlled and tuned either by the plasma power or by the precursor concentration, through which the governing parameters such as composition, particle size, and structure are influenced. As reflected by the measured M-H loops, at discharge power of 1.3 W an increase of precursor concentration from 17.5 to 35 ppm results in lower M_s value for the products. By contrast, at higher powers the same variation in precursor concentration leads to rise in M_s value. This can be ascribed to overall impact from interrelated and competing parameters that together determine the magnetic properties: (1) At low plasma powers the influence of carbon impurities is dominant. Ultrafine Ni nanoparticles (5–15 nm), generated at 1.3 W, are highly active in catalyze C_xH_y species to form carbon atoms. For the lowest studied $Ni(cp)_2$ vapors concentration value of 17.5 ppm, the relatively insufficient carbon supply as well as reduced interactions over hydrocarbon fragments and catalytic surface limit the formation of CNTs impurities in the products. However, as revealed by the OES, the densities of C_xH_y species increase considerably with the $Ni(cp)_2$ concentration. Once the $Ni(cp)_2$ vapors are increased to 35 ppm, the density of dissociated species and the probability of interface contact between hydrocarbon radicals and Ni nanoparticle increase as well, leading to faster carbon acquisition from the gas phase. As a result, the products have higher carbon content, which in turn, resulting in a lower M_s value compared to the nanostructures synthesized at a 17.5 ppm $Ni(cp)_2$ concentration. This is consistent with experimental results, where abundant CNTs were observed at condition 1, but were suppressed at other conditions. (2) When the plasma power is enhanced, the effects of particle size become dominant. Ni nanoparticles generated at high plasma powers are larger and less active in catalyzing hydrocarbon fragments to form CNTs. Therefore,

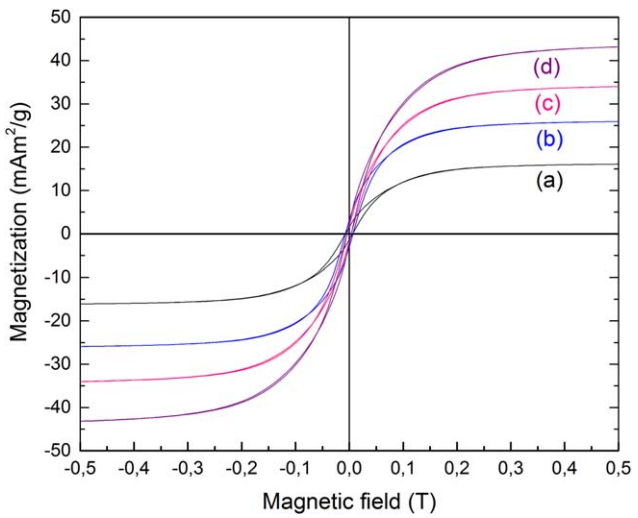

Figure 7. Effect of plasma power on the hysteresis (M-H) loops of products synthesized at 35 ppm $Ni(cp)_2$ vapors: (a) 1.3 W, (b) 2.0 W, (c) 2.7 W, and (d) 3.4 W.

[Color figure can be viewed at wileyonlinelibrary.com]

Table 2. Summary of Processing Parameters of the Existing Approaches for the Gas Phase Ni Nanoparticles Synthesis

	Precursor	Feeding Gas	Temperature (°C)	Pressure (kPa)	Particle Size (nm)	Throughput	Pre/ Posttreatment	Reference
Microplasma	$Ni(C_5H_5)_2$	Ar		101.325	5–25	2.33–4.65 mg/h	no	
CVD	$Ni(CO)_4$	CO, NH_3	575–725	6.89	10–3000	~t/h	Cooling	33,34
CVD	$Ni(CO)_4$	CO, N_2, Ar	260–400	0.01	3–140	0.08–2.2 g/(cm^2·h)	Heating	35,36
CVD	$Ni(C_5H_5)_2$	H_2	490–600	5.33×10^{-6}	60–300		Outgassing	37
CVD	$Ni(C_5H_7O_2)_2$	N_2, H_2	400–500	$0.48\text{-}2.9 \times 10^{-3}$	15–600		Reduction	38
CVD	$Ni(C_5H_4CH_3)_2$	H_2,He	700	5.33×10^{-2}	140–260		Outgassing	39
Laser-assisted	$Ni(CO)_4$	CO, SF_6, Ar	300–350	~83	5–50	140–506 mg/h	Cooling	40
PVD	Ni metal wire	Ar/He	~2300°C	133.3×10^{-3}	15–200	1.91–9.5 g/h	Cooling	41
Arc-plasma	Ni rod	Ar, H_2		100	8–50		Reduction	42
Microwave plasma	$Ni(CO)_4$	Ar/He, CO	3000–11,000 K	34.5–82.7	62–1083	5 kg/h	Cooling	43
Pyrolysis	$NiCI_2$	N_2, H_2	725–1000	10–110	270–630		Cooling, reduction	44,45

much less CNTs are formed, and their influence is considerably reduced. In this situation, the increase of $Ni(cp)_2$ concentration mainly promotes the nucleation and growth of Ni nanoparticles instead of carbon inclusion in the products. Conversely, larger-sized Ni nanoparticles have better magnetic properties, contributing to a further increase of M_s. This hypothesis is supported by the M-H result, where the optimum M_s is achieved at condition 4.

Despite the above results give a proof of principle of the synthesis of Ni nanoparticles with controllable magnetic properties by this facile approach, it is still not clear how $Ni(cp)_2$ vapors are dissociated in the plasma. Moreover, the magnetic behavior of the products is shown to be governed by the operation parameters. To have an idea on the preferential plasma-induced dissociation pathways the $Ni(cp)_2$ molecules, and hopefully to achieve a better control on the products properties by tuning plasma operation conditions, the present study also discusses possible mechanism based on experimental data and relevant information from in-depth literature review (Supporting Information). To our best knowledge, it is the first attempt to provide insight to pathways of this complicated process (Supporting Information Figure S8). Still extensive research is required to fully understand the underlying plasma-induced reaction kinetics and mechanisms.

As described above, the microplasma-assisted process has shown its ability to synthesize Ni nanoparticles with adjustable magnetic properties in a simple, solvent-free, continuous, and one-step manner, which is still regarded as a challenge by the state of technology. This technique combines the advantages of microreactors and the nonthermal plasma chemistry, resulting in a new and facile route for the gas phase fabrication of Ni nanoparticles. Compared to the existing methods (Table 2[33–45]), the present study chooses $Ni(cp)_2$ as the precursor to replace the commonly used $Ni(CO)_4$ which is extremely toxic and dangerous.[36] As a consequence, special safety precautions are not needed. The confinement of the plasma in microspatial scale leads to very high energy density. Ni nanoparticles are produced at the dissipated plasma power as low as ~1.0 W (despite low quantity), which cannot be achieved by the existing approaches. Meanwhile, due to the short residence time ($\sim 10^{-4}$ s, derived from gas flow rate, tube size, and electrode distance) and the uniform RTD of $Ni(cp)_2$ vapors in the plasma, the obtained Ni nanoparticles are much smaller and have narrower size distributions compared with other gas phase processes. Possible side reactions and by-products are considerably suppressed as only the $Ni(cp)_2$ being used as the precursor and dissociated in an inert atmosphere, obviating the use of complex procedures to purify the products. Another distinctive advantage is the demonstrated ability to tune the product properties in-flight by simply adjusting the controlling "knobs" such as the plasma power or the $Ni(cp)_2$ concentration, without any pre/posttreatments like separation, drying or annealing. Thus, the overall synthesis workflow is greatly simplified. Moreover, owing to the versatility of microplasma sources and the high degree of flexibility in processing parameters, this technique is expected to have many promising applications, such as surface modifications or coatings, on-site/direct-write deposition of well-defined nanostructures, fabrication of metal patterns on the polymer films, and in situ formation of patterned electrical conductors.

Conversely, it should be pointed out that the throughput of the current work is not high, as only a single microplasma unit has been applied to fabricate nanoparticles, and the synthesis takes place in a microreactor. The upper limit of the production rate of Ni particles in an assumption of 100% precursor conversion efficiency at 35 ppm $Ni(cp)_2$ vapors by a single plasma jet is calculated as 4.65×10^{-3} g/h. However, the process has the potential to be scaled up by arranging microplasma units in an array structure. One feasible solution is the microjets-array, where a certain number of microplasma jets are arrayed to achieve the parallel operation. We have previously demonstrated that a 2D microjets-array with 100 microplasma jets in each dimension (100×100) can improve the throughput by four orders of magnitude.[46] If such a array was applied to the present study, the production rate is estimated to be 1116 g/day, much higher than the claimed high-throughput synthesis of Ni nanoparticles by a continuous flow method (27 g/day).[47] An alternative way for scaling-up this technique is the so-called planar microdischarges. In such a configuration a matrix of holes are perforated in two planar metallic sheets, which are separated by an insulator. Each hole acts as an independent plasma source after power coupling on the two metal layers.[48] Precursors can be delivered into these holes and being dissociated. Furthermore, the extremely small dimension of the capillaries or the holes results in rather compact reactors. A 2D microjets-array with 100 jets in each dimension is reported be ~1.5 m × 1.5 m, while planar microdischarges with 200 holes only occupies a spatial space of 50 × 50 mm^2, making them attractive for industrial or portable applications.[48]

Regarding the scale-up behavior, for the microjets-array, the sustaining voltage is reported to be the same for each jet while the total current increased by a factor equal to the number of jets. Meanwhile, as each microplasma jet is independent and behaves similarly,[49] it is expected that the product properties of the microjets-array are similar to a single microplasma jet when sustained at the same voltage. More general scaling behavior for a single microplasma reactor as well as for the array of

identical microplasmas is expected to be similar to Yasuda's concept, initially proposed for plasma polymerization.[50] Within this concept the plasma enhanced process is defined by the composite power parameter or process scaling factor W/FM, where W is the discharge wattage, F is the volume flow rate, and M is the molecular weight of the precursor. It should be noted, that in the case of nanostructures growth, in addition to the specific power driven plasma-chemistry scaling (Yasuda parameter), the residence time becomes the key parameter, because together with growth rate it defines the product-size distribution. In turn, the residence time depends on the convective gas flow. Thus, it can be formulated what: the product properties are expected to be similar if (1) the discharge power to total gas flow ratio remains constant, while (2) the concentration of precursor is kept the same. Therefore, to increase throughput and maintain nanoparticle characteristics, the precursor mass flow should be increased, accompanied by the proportional rise in discharge power and carrying gas flow.

Conclusions

In summary, we have introduced a simple, continuous and one step microplasma assisted technique for the gas phase Ni nanoparticle production. Systematic experiments are designed and carried out, for the first time, to establish the relationship between operational conditions and product properties. Innovations of the new route are to give access to less costly and less poisonous reactant, a higher quality product, and a process which is simple, continuous, pre/posttreatment-free with chance for fine-tuning "in-flight." Experimental results show that Ni nanoparticles of controllable magnetic properties are successfully produced, and the upper limit of production rate is calculated as 4.65×10^{-3} g/h for a single plasma jet. The adjusting of plasma power or precursor concentration allows tuning composition, size distribution, morphology, crystal structure and, ultimately, magnetic behavior of the obtained products in a wide range. At relatively low discharge power to precursor mass flow ratio the products contain Ni nanoparticles in both fcc and hcp phases as well as CNTs. It is remarkable that the plasma assisted process can simultaneously result in both metal catalyst nanoparticles and CNTs from one metalorganic precursor. The increase of plasma power led to the inhibition of CNTs growth and preferential formation of fcc Ni with high magnetic properties. Single phase fcc Ni nanoparticles with characteristic size of 20–27 nm and M_s value of 44.4 mAm^2/g are obtained at the optimized condition. Furthermore, based on experimental results and information from literature, a model is proposed to illustrate the possible mechanisms of microplasma assisted nickelocene dissociation process. Finally, microplasma array design is demonstrated as a feasible solution to scale up the technique, and the scale-up behavior of the products is also discussed.

In a broader view, it can be expected that this approach has the potential for practical fabrication of other magnetic nanoparticles, such as cobalt, iron oxide, nickel oxide, and so forth, just by changing precursors and/or adding oxygen in the plasma. The high flexibility and versatility also renders it possible to open up new synthesis route for nanomaterial fabrication in a controlled and environmental friendly manner. In association with the demonstrated adjustable magnetic properties of the products, this can bring critical advantage for medical applications such as cancer hyperthermia treatment.[51] With the advances in microplasma-array technology, it becomes feasible to scale up the throughput of the studied process even towards industrial level by proper design of microplasma array reactors.

Acknowledgments

The authors greatly acknowledge technical assistance and helpful discussions from Ingeborg Schreur (SEM), Anne Spoelstra, Paul Bomans (TEM) and Marco Hendrix (XRD), the Materials and Interface Chemistry Section and the Physical Chemistry Section of Chemical Engineering and Chemistry Department, Eindhoven University of Technology. The authors also acknowledge the support from Chinese Scholarship Council (CSC) and European LIFE12 ENV_NL_000718 "Green plasma process technology for manufacturing of flexible electronics" project.

Literature Cited

1. Fonseca FC, Goya GF, Jardim RF, Muccillo R, Carreño NLV, Longo E, Leite ER. Superparamagnetism and magnetic properties of Ni nanoparticles embedded in SiO_2. *Phys Rev B*. 2002;66(10):104406.
2. Lasheras X, Insausti M, Muro IG, Garaio E, Plazaola F, Moros M, Matteis L, Fuente J, Lezama L. Chemical synthesis and magnetic properties of monodisperse nickel ferrite nanoparticles for biomedical applications. *J Phys Chem C*. 2016;120(6):3492–3500.
3. Veiseh O, Gunn JW, Zhang M. Design and fabrication of magnetic nanoparticles for targeted drug delivery and imaging. *Adv Drug Deliv Rev*. 2010;62(3):284–304.
4. Kang J, Kim Y, Kim H, Hu X, Saito N, Choi J, Lee M. In-situ one-step synthesis of carbon-encapsulated naked magnetic metal nanoparticles conducted without additional reductants and agents. *Sci Rep*. 2016;6(1):38652.
5. Magaye R, Zhao J, Bowman L, Ding M. Genotoxicity and carcinogenicity of cobalt-, nickel- and copper-based nanoparticles. *Exp Ther Med*. 2012;4(4):551–561.
6. Abdelhalim MAK, Mady MM, Ghannam MM. Physical properties of different gold nanoparticles: ultraviolet-visible and fluorescence measurements. *J Nanomed Nanotechnol*. 2012;3(3):1–5.
7. Hufschmid R, Arami H, Ferguson RM, Gonzales M, Teeman E, Brush LN, Browning ND, Krishnan KM. Synthesis of phase-pure and monodisperse iron oxide nanoparticles by thermal decomposition. *Nanoscale*. 2015;7(25):11142–11154.
8. He X, Zhong W, Au CT, Du Y. Size dependence of the magnetic properties of Ni nanoparticles prepared by thermal decomposition method. *Nanoscale Res Lett*. 2013;8(1):446.
9. Chen Y, Peng DL, Lin D, Luo X. Preparation and magnetic properties of nickel nanoparticles via the thermal decomposition of nickel organometallic precursor in alkylamines. *Nanotechnology*. 2007;18(50):505703.
10. Xu X, Lu B, Li F. Formation and catalytic performance of supported Ni nanoparticles via self-reduction of hybrid NiAl-LDH/C composites. *AIChE J*. 2010;56(11):2934–2945.
11. Kumar A, Wolf E, Mukasyan AS. Solution combustion synthesis of metal nanopowders: nickel-reaction pathways. *AIChE J*. 2011;57(8):2207–2214.
12. Dutta J, Hofmann H, Houriet R, Valmalette JC, Hofmeister H. Crystallization of nanosized silicon powder prepared by plasma-induced clustering reactions. *AIChE J*. 1997;43(11A):2610–2615.
13. Lin L, Starostin SA, Hessel V, Wang Q. Synthesis of iron oxide nanoparticles in microplasma under atmospheric pressure. *Chem Eng Sci*. 2017;168:360–371.
14. Lin L, Wang Q. Microplasma: a new generation of technology for functional nanomaterial synthesis. *Plasma Chem Plasma Process*. 2015;35(6):925–962.
15. Chiang WH, Sakr M, Gao XPA, Sankaran RM. Nanoengineering Ni_xFe_{1-x} catalysts for gas-phase, selective synthesis of semiconducting single-walled carbon nanotubes. *ACS Nano*. 2009;3(12):4023–4032.
16. Eusebio MTV, Rojas A. Vapor pressures and sublimation enthalpies of nickelocene and cobaltocene measured by thermogravimetry. *J Chem Eng Data*. 2011;56(12):5008–5018.
17. Ghosh S, Liu T, Bilici M, Cole J, Huang I-M, Staack D, Mariotti D, Sankaran RM. Atmospheric-pressure dielectric barrier discharge with capillary injection for gas-phase nanoparticle synthesis. *J Phys D Appl Phys*. 2015;48(31):314003.
18. Crintea DL, Czarnetzki U, Iordanova S, Koleva I, Luggenhölscher D. Plasma diagnostics by optical emission spectroscopy on argon

and comparison with Thomson scattering. *J Phys D Appl Phys*. 2009;42(4):045208.
19. Lin PA, Kumar A, Sankaran RM. New insights into plasma-assisted dissociation of organometallic vapors for gas-phase synthesis of metal nanoparticles. *Plasma Process Polym*. 2012;9(11–12):1184–1193.
20. Jain DC. Transition probability parameters of the swan and the Fox-Herzberg band systems of the C_2 molecule. *J Quant Spectrosc Radiat Transf*. 1964;4(3):427–440.
21. Pearse RWB, Gaydon AG. *The Identification of Molecular Spectra*, 3rd ed. London: Chapman and Hall, 1963.
22. Wang SB, Lei GJ, Liu DP, Yang S. Balmer H_α, H_β and H_γ special lines intensities in high-power RF hydrogen plasmas. *Plasma Sci Technol*. 2014;16(3):219–222.
23. National Institute of Standards and Technology. Atomic Spectra Database. Available at: https://www.nist.gov/pml/atomic-spectra-database. 2016.
24. Wolfer M, Kriele A, Williams OA, Obloh H, Leancu CC, Nebel CE. Nickel doping of nitrogen enriched CVD-diamond for the production of single photon emitters. *Phys Status Solidi Appl Mater Sci*. 2009; 206(9):2012–2015.
25. Beha K, Fedder H, Wolfer M, Becker MC, Siyushev P, Jamali M, Batalov A, Hinz C, Hees J, Kirste L, Obloh H, Gheeraert E, Naydenov B, Jakobi I, Dolde F, Pezzagna S, Twittchen D, Markham M, Dregely D, Giessen H, Meijer J, Jelezko F, Nebel CE, Bratschitsch R, Leitenstorfer A, Wrachtrup J. Diamond nanophotonics. *Beilstein J Nanotechnol*. 2012;3(1):895–908.
26. Wang YH, Chiu SC, Lin KM, Li YY. Formation of carbon nanotubes from polyvinyl alcohol using arc-discharge method. *Carbon*. 2004;42(12–13):2535–2541.
27. Chinnasamy CN, Jeyadevan B, Shinoda K, Tohji K, Narayanasamy A, Sato K, Hisano S. Synthesis and magnetic properties of face-centered-cubic and hexagonal-close-packed Ni nanoparticles through polyol process. *J Appl Phys*. 2005;97(10):10J309.
28. Mireille RP, Guillot M, Vilminot S, Leuvrey C, Estournès C, Kurmoo M. Hcp and fcc nickel nanoparticles prepared from organically functionalized layered phyllosilicates of nickel(II). *Chem Mater*. 2007;19(4):865–871.
29. Han M, Liu Q, He J, Song Y, Xu Z, Zhu J. Controllable synthesis and magnetic properties of cubic and hexagonal phase nickel nanocrystals. *Adv Mater*. 2007;19(8):1096–1100.
30. Jeon YT, Moon JY, Lee GH, Park J, Chang Y. Comparison of the magnetic properties of metastable hexagonal close-packed Ni nanoparticles with those of the stable face-centered cubic Ni nanoparticles. *J Phys Chem B*. 2006;110(3):1187–1191.
31. Chiang WH, Sankaran RM. Relating carbon nanotube growth parameters to the size and composition of nanocatalysts. *Diam Relat Mater*. 2009;18(5–8):946–952.
32. Li Y, Kim W, Zhang Y, Rolandi M, Wang D, Dai H. Growth of single-walled carbon nanotubes from discrete catalytic nanoparticles of various sizes. *J Phys Chem B*. 2001;105(46):11424–11431.
33. Wasmund EB, Saberi S, Coley KS. Modeling of an aerosol reactor for optimizing product properties. *AIChE J*. 2007;53(6):1429–1440.
34. Wasmund EB, Coley KS. In situ sampling uncovers the dynamics of particle genesis and growth in an aerosol tube reactor. *J Mater Sci*. 2006;41(21):7103–7110.
35. Kauffeldt E, Kauffeldt T. Thermodynamic-controlled gas phase process for the synthesis of nickel nanoparticles of adjustable size and morphology. *J Nanopart Res*. 2006;8(3–4):477–488.
36. Carlton HE, Oxley JH. Kinetics of the heterogeneous decomposition of nickel tetracarbonyl. *AIChE J*. 1967;13(1):86–91.
37. Stauf GT, Driscoll DC, Dowben PA, Barfuss S, Grade M. Iron and nickel thin film deposition via metallocene decomposition. *Thin Solid Films*. 1987;153(1–3):421–430.
38. Moravec P, Smolík J, Keskinen H, Mäkelä JM, Bakardjieva S, Levdansky VV. NiO_x nanoparticle synthesis by chemical vapor deposition from nickel acetylacetonate. *Mater Sci Appl*. 2011;2:258–264.
39. Fraser B, Hampp A, Kaesz HD. Controlled growth of Ni particles on Si (100). *Chem Mater*. 1996;8(100):1858–1864.
40. He Y, Li X, Swihart MT, York N. Laser-driven aerosol synthesis of nickel nanoparticles. *Chem Mater*. 2005;17(5):1017–1026.
41. Morozov YG, Belousova OV, Kuznetsov MV. Preparation of nickel nanoparticles for catalytic applications. *Inorg Mater*. 2011;47(1):36–40.
42. Duan H, Lin X, Liu G, Xu L, Li F. Synthesis of Ni nanoparticles and their catalytic effect on the decomposition of ammonium perchlorate. *J Mater Process Technol*. 2008;208(1–3):494–498.
43. Paserin V, Richard SA, Boulos MI, Jurewicz J, Guo J. Inco Limited Toronto Ontario, Tekna plasma systems, Inc., Sherbrooke, Quebec. Method producing metal nanopowders by decompositon of metal carbonyl using an induction plasma torch. US 7967891 B2, 2011.
44. Okada Y, Matsumoto S, Sawai R, Kinoshita T. Formation of non-aggregated nickel nanoparticles for catalysts by gas-phase reaction. *J Chem Eng Jpn*. 2017;50(7):511–515.
45. Stopic S, Ilic I, Uskokovic D. Structural and morphological transformations during NiO and Ni particles generation from chloride precursor by ultrasonic spray pyrolysis. *Mater Lett*. 1995;24(6):369–376.
46. Lin L, Starostin SA, Wang Q, Hessel V. An atmospheric pressure microplasma process for continuous synthesis of titanium nitride nanoparticles. *Chem Eng J*. 2017;321:447–457.
47. Roberts EJ, Habas SE, Wang L, Ruddy DA, White EA, Baddour FG, Griffin MB, Schaidle JA, Malmstadt N, Brutchey RL. High-throughput continuous flow synthesis of nickel nanoparticles for the catalytic hydrodeoxygenation of guaiacol. *ACS Sustain Chem Eng*. 2017;5(1):632–639.
48. Penache C, Bräuning-Demian CGA, Scheffler P, Spielberger L, Hohn O, Schössler S, Jahnke T, Gericke KH, Schmidt-Böcking H. Micro-structured electrode arrays: a source of high-pressure non-thermal plasma. Selected research papers on spectroscopy of non-equilibrium plasma at elevated pressures, 2002, Moscow, Russian Federation.
49. Sankaran RM, Giapis KP. Hollow cathode sustained plasma microjets: characterization and application to diamond deposition. *J Appl Phys*. 2002;92(5):2406–2411.
50. Yasuda H. *Plasma Polymerization*. Orlando, Florida: Academic Press, 1985.
51. Wu J, Zhou W, Cheng Q, Yang J. Polyvinylpyrrolidone-stabilized magnetic nickel nanochains for cancer hyperthermia and catalysis applications. *RSC Adv*. 2015;5(29):22965–22971.

Manuscript received June 19, 2017, and revision received Dec. 7, 2017.